



HAL
open science

Assessing the effective elastic properties of the tendon-to-bone insertion: a multiscale modeling approach

A. Aghaei, N. Bochud, G. Rosi, S. Naili

► To cite this version:

A. Aghaei, N. Bochud, G. Rosi, S. Naili. Assessing the effective elastic properties of the tendon-to-bone insertion: a multiscale modeling approach. *Biomechanics and Modeling in Mechanobiology*, 2021, 20 (2), pp.433-448. 10.1007/s10237-020-01392-7 . hal-03208707

HAL Id: hal-03208707

<https://hal.science/hal-03208707>

Submitted on 26 Apr 2021

HAL is a multi-disciplinary open access archive for the deposit and dissemination of scientific research documents, whether they are published or not. The documents may come from teaching and research institutions in France or abroad, or from public or private research centers.

L'archive ouverte pluridisciplinaire **HAL**, est destinée au dépôt et à la diffusion de documents scientifiques de niveau recherche, publiés ou non, émanant des établissements d'enseignement et de recherche français ou étrangers, des laboratoires publics ou privés.

Assessing the effective elastic properties of the tendon-to-bone insertion: A multiscale modeling approach

A. Aghaei^{a,b}, N. Bochud^{a,b,*}, G. Rosi^{a,b}, S. Naili^{a,b}

^a*Univ Paris Est Creteil, CNRS, MSME, F-94010 Creteil, France*

^b*Univ Gustave Eiffel, MSME, F-77454 Marne-la-Vallée, France*

Abstract

The interphase joining tendon to bone plays the crucial role of integrating soft to hard tissues, by effectively transferring stresses across two tissues displaying a mismatch in mechanical properties of nearly two orders of magnitude. The outstanding mechanical properties of this interphase are attributed to its complex hierarchical structure, especially by means of competing gradients in mineral content and collagen fibers organization at different length scales. The goal of this study is to develop a multiscale model to describe how the tendon-to-bone insertion derives its overall mechanical behavior. To this end, the effective anisotropic stiffness tensor of the interphase is predicted by modeling its elastic response at different scales, spanning from the nanostructural to the mesostructural levels, using continuum micromechanics methods. The results obtained at a lower scale serve as inputs for the modeling at a higher scale. The obtained predictions are in good agreement with stochastic finite element simulations and experimental trends reported in literature. Such model has implication for the design of bioinspired bi-materials that display the functionally graded properties of the tendon-to-bone insertion.

Keywords: Tendon-to-bone insertion, Homogenization, Continuum micromechanics, Biological interphase, Functionally graded material, Partially mineralized tissue

*Corresponding author: nicolas.bochud@u-pec.fr

1. Introduction

The interaction between soft and hard tissues is essential to ensure good mobility to the musculoskeletal system. Specifically, the integration between tendon (or ligament) and bone occurs through a particular tissue interphase called *enthesis*, which derives from the ancient Greek word referring to the insertion. According to their musculoskeletal site of insertion, entheses can be characterized as fibrous or fibrocartilaginous [1]. Fibrous (or indirect) insertions are usually found where tendons and ligaments attach to the shaft of long bones, such as the insertion of the deltoid tendon into the humerus or the tibial insertion of the medial collateral ligament. Fibrocartilaginous (or direct) insertions are more common and present at the bony attachments of the rotator cuff, the anterior cruciate ligament and the Achilles tendons. Fibrocartilaginous insertions are generally divided into four distinct regions with different compositions, functions, and biomechanical properties: (1) the tendon, which consists of aligned type I collagen fibers with a small amount of non-collagenous proteins (NCPs), including proteoglycans and the remaining volume filled with water [2]; (2) a non-mineralized fibrocartilaginous region, which is an avascular zone consisting of unmineralized types I, II and III collagen fibers and proteoglycan aggrecan [3]; (3) a mineralized fibrocartilaginous region, which is mostly characterized by partially mineralized type II collagen fibers, the proteoglycan aggrecan being produced by fibrocartilage cells or fibrochondrocytes between bundles of collagen fibers [4]; and (4) the bone, which is a composite material that mainly consists of highly mineralized type I collagen [5].

Although these different tissue regions are compositionally distinct, they are structurally continuous. Moreover, it is acknowledged that the mechanical environment of the enthesis is complex and heterogeneous, as it is subject to tensile, compressive and shear forces [6], in order to ensure an effective transfer of the mechanical stresses across the two surrounding tissues, which show a mismatch in mechanical properties of nearly two orders of magnitude. Three main features contribute to the mechanical effectiveness of the enthesis: (1) its geometry is characterized by a shallow attachment angle and an optimized shape of the outward splay, which improves its resistance to mechanical loads [7]; (2) the interdigitation of the

29 bone within the tendon, described as a wave-like structure, allows a gain in toughness, as
30 well as a better distribution of stresses on the fraction of tissue implied in this mechanism
31 [8]; and (3) a compositional and structural gradient, through a gradual increase in mineral
32 content together with a corresponding reorganization of the collagen fibers from the tendon
33 to the bone [9]. The combination of these multiscale factors is hypothesized to lead to an
34 intermediate zone more compliant than either tendon or bone, thus ensuring an effective
35 distribution of mechanical stresses, which allows reducing the risk of rupture [10, 11].

36 Musculoskeletal injuries involving tendon rupture typically require surgical reattachment
37 back to bone. Such operations exhibit a high rate of failure because the enthesis rarely
38 regenerates and does not recover its mechanical properties. This clinical burden is mainly
39 due to the lack of understanding of the healthy attachment, as well as of the damaging
40 process that may occur at this interphase [12]. To date, studies on the tendon-to-bone
41 insertion have mainly focused on the rehabilitation methods to be implemented after a
42 tendon operation, as well as on the histology of the enthesis [13]. The targeted parameters
43 generally included compositional and structural features at lower length scales (*e.g.*, collagen
44 types, organization and morphology of collagen fibers, degree of mineralization), but seldom
45 the mechanical properties at the tissue scale. Indeed, the direct mechanical measurement of
46 the tendon-to-bone insertion has been shown to be very complicated, particularly because
47 of its heterogeneity and small dimensions (typically a few μm to some mm according to the
48 insertion site) [10, 14]. The excellent mechanical properties of the enthesis are attributed to
49 its complex hierarchical structure. Nonetheless, understanding how this hierarchy and the
50 resulting mechanical properties at the different scales affect its overall mechanical behavior
51 and allow such an effective stress transfer across this interphase represents a considerable
52 challenge. To address this issue, tools such as multiscale modeling could help predicting
53 the effective stiffness properties of the enthesis at the tissue level, as well as studying the
54 individual impact of lower-scale features on its overall mechanical behavior at higher scales.

55 Regardless of the considered medium –tendon, enthesis or bone–, all these regions sub-
56 stantially have a similar hierarchical collagen-based structure starting with collagen molecules
57 at the nanoscale up to a pattern of collagen fibers surrounded by an extracellular matrix at

58 higher scales [15]. Several analytical and computational models have been proposed to infer
59 the mechanical properties of bone at different scales, in particular using homogenization
60 methods [16–19]. In the same way, a few studies have been conducted on the hierarchical
61 modeling of (mineralized) tendon [20, 21]. However, little information concerning the multi-
62 scale modeling of the tendon-to-bone insertion is available in the literature. Biomechanical
63 models were initially proposed by considering the collagen-mineral interactions and the col-
64 lagen fiber architecture at the microscale. In a pioneering study, Genin *et al.* [22] estimated
65 the stiffness of partially mineralized fibers by randomly distributing minerals among un-
66 mineralized cylindrical collagen fibrils using Monte Carlo simulations, which subsequently
67 allowed determining the isotropic mechanical properties of the partially mineralized tissue at
68 the macroscale. Later, the same group introduced a progressive stiffening model for collagen,
69 by accounting for different sequences of mineral accumulation across spatial hierarchy levels
70 spanning from the fibril to the tissue level, to estimate the mechanical properties of par-
71 tially mineralized collagen tissue [23]. In a subsequent study, they presented an estimate for
72 composites containing multiple classes of aligned ellipsoidal inclusions with a relatively high
73 volume fraction, which demonstrated its potential application to the graded tissue inter-
74 phase at the tendon-to-bone attachment [24]. More recently, the micromechanical behavior
75 of tendon-to-bone structures was studied and compared with a composite beam-bending
76 model [25]. The beam was modeled as a three-phase composite in series, in which the
77 modulus of the transitional graded interphase was defined as a linear extrapolation between
78 those of the mineralized and unmineralized regions. All these models provided a general
79 understanding on the mechanical properties of the insertion site (*i.e.*, average Young mod-
80 ulus) at different structural levels. However, to the best of our knowledge, these models
81 only partially accounted for the anisotropic nature of the interphase at the different scales,
82 and the transition between different hierarchies from the nanoscale to the mesoscale was
83 not achieved. Moreover, the impact of the individual nanoscale properties on the effective
84 stiffness tensor at the mesoscale was not addressed so far.

85 To face these current limitations, this study aims at developing a hierarchical model to
86 predict the effective anisotropic stiffness tensor of the tendon-to-bone insertion by model-

ing its elastic response at different scales spanning from the nano- to the mesostructural levels. To this end, a continuum micromechanics approach was proposed by distinguishing six homogenization steps at four different scales. First, we derived the effective stiffness properties of the enthesis at the mesoscale by accounting for gradients in mineral content and collagen fibers organization across the interphase at lower scales. Second, we carried out a parametric study to evaluate the impact of the mechanical properties of each nanoscale component on the overall mechanical behavior of the insertion site. Third, based on the knowledge of the mechanical properties of the two surrounding tissues at the mesoscale, an optimization procedure was solved to identify the nanoscale properties that yield the best agreement between the model predictions and ultrasonic data reported in the literature. Numerical results show that the effective mechanical properties predicted by our multiscale model are in good agreement with earlier modeling approaches and experimentally observed trends. Moreover, our model is straightforward and could be readily extended to account for damage characteristics of the interphase as a footprint of clinical burden.

The paper is structured as follows: Sec. 2 recalls the fundamentals of micromechanics-based models and introduces the proposed multiscale modeling of the enthesis. The model parameters, *i.e.*, the mechanical properties, volume fractions and gradients of the tendon-to-bone insertion's components, are then described in Sec. 3. Finally, the numerical results are presented in Sec. 4 and discussed in the light of the literature in Sec. 5.

2. Methods

In this section, a multiscale model of the tendon-to-bone insertion based on a hierarchical modeling approach that consists of successive homogenization steps from the nanostructural to the mesostructural levels is proposed. This multiscale model relies on several hypotheses: (1) whereas mineral grading can occur at any length scale, it was incorporated here at the nanoscale [26]; (2) the gradient in collagen fibers organization occurred at the microscale [22]; (3) type I collagen was assumed to be the main organic component across the interphase; and (4) the mechanical properties of the elementary nanoscale components (collagen, hydroxyapatite (HA), water and NCPs), which were used as input data in our model, were all

115 assumed to have a linear elastic and isotropic behavior.

116 2.1. Fundamentals of micromechanics-based models

117 Continuum micromechanics allows estimating the effective stiffness properties of heteroge-
 118 neous materials [27], which can generally be derived by solving the matrix-inclusion problem
 119 according to Eshelby [28]. A basic concept of continuum micromechanics consists in selecting
 120 a representative volume element (RVE) in the structure. Based on the separation-of-scales
 121 requirement, the characteristic length ℓ of this RVE must be considerably larger than the
 122 dimension of the heterogeneities d within the RVE and implicitly smaller than the charac-
 123 teristic length of the structure \mathcal{L} , so that $d \ll \ell \ll \mathcal{L}$. Useful information concerns volume
 124 fractions and elastic properties of phases, the existence of one connected matrix phase in
 125 which one or several inclusion phases with different shapes are embedded or the disordered
 126 arrangement of all phases. Hence, the homogenized stiffness tensor of such RVE, \mathbb{C}_{hom} , can
 127 be stated as in [29]

$$\mathbb{C}_{\text{hom}} = \sum_{r=1}^n f_r \mathbb{c}_r : [\mathbb{I} + \mathbb{P}_r^0 : (\mathbb{c}_r - \mathbb{C}^0)]^{-1} : \left\{ \sum_{s=1}^n f_s [\mathbb{I} + \mathbb{P}_s^0 : (\mathbb{c}_s - \mathbb{C}^0)]^{-1} \right\}^{-1} \quad (1)$$

128 where $:$ denotes the double contracted product of two tensors, n is the number of phases
 129 in the RVEs, f_r denotes the volume fraction of the phase r , \mathbb{I} is the fourth-order identity
 130 tensor, \mathbb{c}_r is the stiffness tensor of phase r , \mathbb{C}^0 is the stiffness tensor of the matrix phase, and
 131 \mathbb{P}^0 is the so-called Hill tensor of phase r embedded in the matrix phase, whose form depends
 132 on the shape of the inclusion and on the stiffness tensor of the surrounding matrix \mathbb{C}^0 . The
 133 Hill tensor can be related to the Eshelby tensor as $\mathbb{P}^0 = \mathbb{S}_{\text{Esh}}^0 : (\mathbb{C}^0)^{-1}$. The components
 134 of the Hill tensors for the different inclusion shapes considered in this study are provided
 135 in [Appendix A](#).

136 Several approaches for determining \mathbb{C}^0 have been proposed in the literature. Among
 137 these, two methods are particularly relevant to our context. First, the Mori-Tanaka scheme
 138 can be applied when the inclusion phase consists of small particles surrounded by a contin-
 139 uous homogeneous matrix [30]. In such a case, the matrix phase can be directly identified
 140 as the actual matrix phase (*i.e.*, $\mathbb{C}^0 = \mathbb{C}_{\text{matrix}}$). Second, when no matrix phase can be

141 clearly identified, it is convenient to apply the self-consistent scheme [31]. The underlying
142 hypothesis of this second method consists in estimating the homogenized properties of the
143 effective medium by locating each inhomogeneity in the homogeneous effective medium (*i.e.*,
144 $\mathbb{C}^0 = \mathbb{C}_{\text{hom}}$).

145 2.2. Multiscale modeling of the tendon-to-bone insertion

146 According to earlier studies applied to partially mineralized tissues, such as bone [17, 32, 33]
147 and mineralized tendon [20], we hierarchically modeled here the mechanical behavior of the
148 tendon-to-bone insertion by considering four relevant hierarchical levels compound of six
149 homogenization steps (see Fig. 1), and by assuming gradients in mineral content and colla-
150 gen fibers organization across the interphase between the two surroundings tissues [22, 23].
151 Across the enthesis, mineral crystals replace the water by filling the gap zones between
152 collagen thereafter spreading through the fibrils surface [34]. Extrapolating this considera-
153 tion to our modeling approach, the fibril array was considered as a hydrated collagen fibril
154 at the nanoscale (i) without mineral particles in the tendon region, (ii) with a functional
155 grading of mineral across the insertion, and (iii) as a partially mineralized collagen fibril
156 in the bone region. The gradient of mineralization was introduced in the model by means
157 of a normalized mineral volume fraction, $\phi(x)$, defined as the ratio of the overall mineral
158 volume fraction $f_{\text{mineral}}(x)$ at a normalized position along the insertion, x , to the overall
159 volume fraction of mineral at the bone level, $f_{\text{mineral}}^{\text{bone}}$, so that $\phi(x) = f_{\text{mineral}}(x)/f_{\text{mineral}}^{\text{bone}}$. The
160 normalized position x across the interphase was thus $x = 0$ at the end of the tendon (*i.e.*,
161 $\phi(x) = 0$) and $x = 1$ at the beginning of the bone (*i.e.*, $\phi(x) = 1$), so that $\phi(x) \approx x$.
162 Moreover, the gradient in collagen fibers organization was accounted for by considering the
163 angular deviation of the collagen fibers distribution at a normalized position x along the
164 insertion [22]. At each scale, the homogenized stiffness tensor of the enthesis, $\mathbb{C}_{\text{hom}}(x)$, was
165 therefore related to a precise description of the geometric and mechanical properties of each
166 of the subscales at any normalized position x across the interphase.

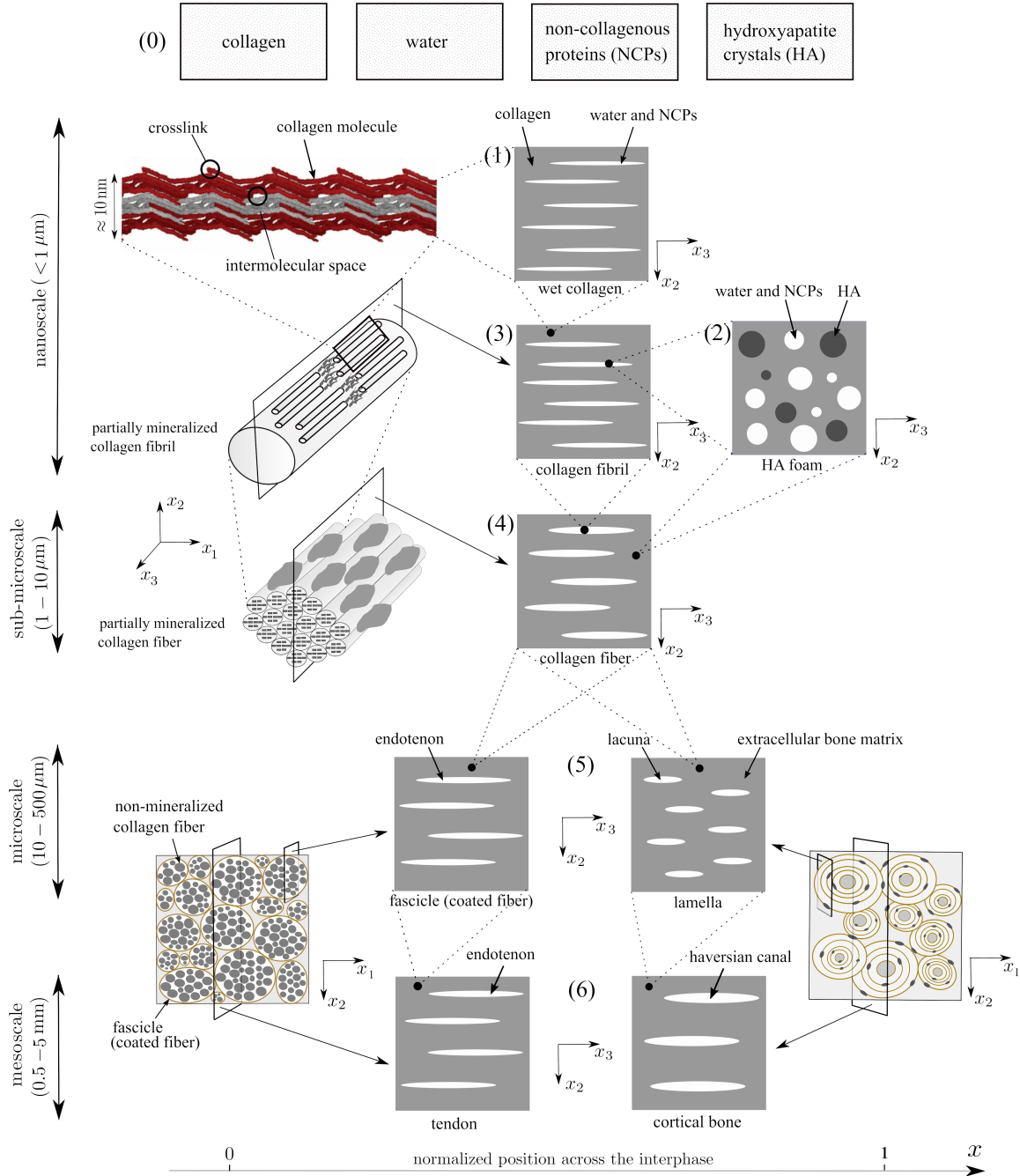


Figure 1: Successive steps of our multiscale modeling approach: (0) elementary nanoscale components; (1) wet collagen composite formed by a collagen molecules matrix containing water and NCPs-filled pores (image adapted from [35]); (2) HA foam formed by HA crystals containing water and NCPs-filled pores; (3) partially mineralized collagen fibril made up from wet collagen and intrafibrillar HA foam; (4) partially mineralized collagen fiber formed by partially mineralized collagen fibrils and extrafibrillar HA foam; (5) lamella and unit fascicle built up from a partially mineralized collagen fiber matrix holding lacunae cavities and *endotenon*, respectively; and (6) cortical bone and tendon formed by a continuous bone matrix (extravascular bone) and a bundle of parallel fascicles matrix containing haversian canals and *endotenon*, respectively.

167 *A. Nanostructural level*

168 At the nanostructural level, collagen molecules are attached to each other by crosslinks,
 169 which transfer the stresses from one collagen molecule to another [35]. Water initially fills the
 170 spaces between collagen molecules. During the mineralization process, mineral crystals are
 171 nucleated in the gap zones, thus progressively replacing the water. They then further grow
 172 into the overlap zones during development and may be distributed throughout the collagen
 173 molecules to form a partially mineralized collagen fibril [36]. To mimic this physiological
 174 process, three homogenization steps were used to model the entheses at the nanostructural
 175 level: (1) combining collagen together with water and NCPs, (2) combining HA crystals
 176 with water and NCPs, and (3) combining the collagen composite from step 1 with the HA
 177 foam from step 2 to form a partially mineralized collagen fibril.

178 *Step 1: wet collagen composite*

179 The wet collagen composite was modeled as a contiguous cross-linked collagen molecules
 180 matrix with holes hosting water and NCPs, where the holes were considered as cylindrical
 181 inclusions [33, 37]. Based on the assumption that a continuum approach can be applied at
 182 the nanostructural level, the Mori-Tanaka scheme was used to estimate the effective stiffness
 183 tensor of the composite, \mathbb{C}_{wc} , at this scale as

$$\begin{aligned} \mathbb{C}_{\text{wc}} = & (1 - f_{\text{wp}})\mathbb{C}_{\text{col}} + f_{\text{wp}}\mathbb{C}_{\text{wp}} : \left[\mathbb{I} + \mathbb{P}_{\text{wp}}^{\text{col}}(\mathbb{C}_{\text{wp}} - \mathbb{C}_{\text{col}}) \right]^{-1} \\ & : \left\{ (1 - f_{\text{wp}})\mathbb{I} + f_{\text{wp}} \left[\mathbb{I} + \mathbb{P}_{\text{wp}}^{\text{col}} : (\mathbb{C}_{\text{wp}} - \mathbb{C}_{\text{col}}) \right]^{-1} \right\}^{-1}, \end{aligned} \quad (2)$$

184 where subscripts “wc”, “col” and “wp” are referred to the wet collagen composite, collagen,
 185 and water-protein mixture, respectively.

186 *Step 2: hydroxyapatite foam*

187 At the scale of a few hundred nanometers, HA crystals were assumed to be interpenetrated
 188 by intercrystalline space filled with water and NCPs [19]. Since no well-defined matrix
 189 phase can be identified at this scale, it results convenient to apply the self-consistent scheme
 190 to estimate the effective stiffness tensor of the HA foam, $\mathbb{C}_{\text{Hw}}(x)$, which depends upon the
 191 mineral gradient across the insertion. Both the mineral phase and the water-protein mixture

192 were here assumed to be spherical in shape with a linear elastic and isotropic behavior.

193 Hence,

$$\mathbb{C}_{\text{Hw}}(x) = \sum_{r=1}^2 f_r(x) \mathbb{C}_r : [\mathbb{I} + \mathbb{P}_r^0 : (\mathbb{C}_r - \mathbb{C}_{\text{Hw}}(x))]^{-1} : \left\{ \sum_{s=1}^2 f_s(x) [\mathbb{I} + \mathbb{P}_s^0 : (\mathbb{C}_s - \mathbb{C}_{\text{Hw}}(x))]^{-1} \right\}^{-1}, \quad (3)$$

194 with $r, s \in [\text{HA}, \text{wp}]$. The subscript ‘‘Hw’’ denotes the HA foam. The detailed calculation
195 of the stiffness coefficients is provided in [Appendix B](#).

196 *Step 3: partially mineralized collagen fibril*

197 The collagen fibril structure was modeled as a composite consisting of a wet collagen com-
198 posite matrix reinforced with aligned needle-shaped interfibrillar minerals, which were as-
199 sumed to be distributed along the main axis of the collagen fibril [38]. Again, the classical
200 Mori-Tanaka method was applied to determine the effective stiffness tensor of a partially
201 mineralized collagen fibril, $\mathbb{C}_{\text{fib}}(x)$, as

$$\begin{aligned} \mathbb{C}_{\text{fib}}(x) &= (1 - f_{\text{Hw}}) \mathbb{C}_{\text{wc}} + f_{\text{Hw}} \mathbb{C}_{\text{Hw}}(x) : [\mathbb{I} + \mathbb{P}_{\text{Hw}}^{\text{wc}} : (\mathbb{C}_{\text{Hw}}(x) - \mathbb{C}_{\text{wc}})]^{-1} \\ &: \left\{ (1 - f_{\text{Hw}}) \mathbb{I} + f_{\text{Hw}} [\mathbb{I} + \mathbb{P}_{\text{Hw}}^{\text{wc}} : (\mathbb{C}_{\text{Hw}}(x) - \mathbb{C}_{\text{wc}})]^{-1} \right\}^{-1}, \end{aligned} \quad (4)$$

202 where \mathbb{C}_{wc} and $\mathbb{C}_{\text{Hw}}(x)$ are the effective stiffness tensors resulting from the application of
203 steps 1 and 2, respectively.

204 *B. Sub-microstructural level – partially mineralized collagen fiber*

205 At the scale of several micrometers (step 4), randomly dispersed extrafibrillar minerals with
206 different sizes and shapes strongly adhere to the outer parts of the collagen fibrils [34]. During
207 the mineralization, these extrafibrillar minerals are located around the fibril surface and then
208 start growing along the main fibril axis, therefore forming a sort of reinforcing structure
209 around the fibril. Consequently, a partially mineralized collagen fiber can be modeled as
210 an extrafibrillar HA foam matrix pervaded by a cylindrical collagen fibril inclusion. In this
211 way, the effective stiffness tensor of the partially mineralized collagen fiber, $\mathbb{C}_{\text{fbr}}(x)$, can be

212 estimated using the Mori-Tanaka scheme as

$$\begin{aligned} \mathbb{C}_{\text{fbr}}(x) &= (1 - f_{\text{fib}})\mathbb{C}_{\text{Hw}}(x) + f_{\text{fib}}\mathbb{C}_{\text{fib}}(x) : \left[\mathbb{I} + \mathbb{P}_{\text{fib}}^{\text{Hw}}(x) : (\mathbb{C}_{\text{fib}}(x) - \mathbb{C}_{\text{Hw}}(x)) \right]^{-1} \\ &: \left\{ (1 - f_{\text{fib}})\mathbb{I} + f_{\text{fib}} \left[\mathbb{I} + \mathbb{P}_{\text{fib}}^{\text{Hw}}(x) : (\mathbb{C}_{\text{fib}}(x) - \mathbb{C}_{\text{Hw}}(x)) \right]^{-1} \right\}^{-1}, \end{aligned} \quad (5)$$

213 where $\mathbb{C}_{\text{Hw}}(x)$ and $\mathbb{C}_{\text{fib}}(x)$ are the effective stiffness tensors resulting from the application of
214 steps 2 and 3, respectively.

215 Moving from the tendon to bone, apart from the gradual increase in mineral content
216 (already accounted for in step 2), the insertion site also shows a gradual decrease in the
217 organization of collagen fibers. At the tendon level, collagen fibers are aligned and parallelly-
218 oriented along the x_3 -axis. These then start bending and intercrossing along the insertion,
219 and become less organized near the bone [9]. Consequently, the effective stiffness tensor of an
220 individual partially mineralized collagen fiber, $\mathbb{C}_{\text{fbr}}(x)$, can be related to the microstructural
221 level (*i.e.*, fiber bundle or pattern) by averaging over the fibers orientation at each position
222 x of the insertion. Hence,

$$\bar{\mathbb{C}}_{\text{fbr}}(x) = \int_S (\mathbb{R}(\mathbf{n})\mathbb{C}_{\text{fbr}}(x)\mathbb{R}^T(\mathbf{n})) p(\mathbf{n}, s(x)) dS \quad (6)$$

223 where the superscript T denotes the transpose operator; $p(\mathbf{n}, s(x))$ is an axisymmetric and
224 spherical probability density function for finding a fiber whose axis is parallel to the unit
225 vector \mathbf{n} , with $s(x)$ the angular deviation at a position x with respect to the mean fiber
226 direction x_3 ; $\mathbb{R}(\mathbf{n})$ rotates a tensor from this coordinate system into the global coordinate
227 system; and \mathbf{n} includes all directions over the unit sphere S [22]. Note that the resulting
228 stiffness tensor of a partially mineralized fibers pattern, $\bar{\mathbb{C}}_{\text{fbr}}(x)$, retains the symmetry class
229 of that of an individual collagen fiber, but results more compliant along the x_3 -direction.

230 *C. Microstructural level – partially mineralized fibers pattern*

231 At the microstructural level (step 5), the structure and composition of tendon and bone
232 are no longer identical, and therefore lead to a different approach for modeling a partially
233 mineralized fibers pattern. At the tendon level, a bundle of aligned collagen fibers forms a
234 unit fascicle, which represents the basic unit of a tendon. A thin connective tissue called

235 *endotenon* surrounds each collagen fiber and binds the fibers together [39]. Since the self-
 236 consistent and Mori-Tanaka methods are limited to an inclusion associated with a low volume
 237 fraction, the interactions between neighboring fibers cannot be neglected anymore [24]. To
 238 circumvent this issue, the so-called “inverse Mori-Tanaka” scheme was applied here simply
 239 by inverting the matrix and inclusion phases [17]. In this regard, by considering the con-
 240 nected bundle of collagen fibers as a matrix and *endotenon* as a cylindrical inclusion, the
 241 effective stiffness tensor of a unit fascicle can be estimated. At the bone level, a lamella
 242 containing cavities filled with osteocytes called *lacunae* is enclosed by the continuous bone
 243 matrix holding a bundle of preferentially oriented collagen fibers. In addition, the main axis
 244 of *lacunae* was assumed to be oriented along the longitudinal direction of a lamella [40].
 245 Therefore, similarly to the tendon region, the effective stiffness tensor of a lamella can be
 246 estimated by considering the *lacuna* as a cylindrical inclusion coated with a continuous bone
 247 matrix. Hence, the effective stiffness tensor of a partially mineralized fibers pattern at the
 248 microstructural level, $\mathbb{C}_{\text{mic}}(x)$, was estimated by considering $\mathbb{C}^0 \equiv \mathbb{C}_{\text{end}} \equiv \mathbb{C}_{\text{lac}} \equiv \mathbb{C}_{\text{wp}}$, so
 249 that

$$\begin{aligned}
 \mathbb{C}_{\text{mic}}(x) = & f_{\text{fbr}}(x)\bar{\mathbb{c}}_{\text{fbr}}(x) + (1 - f_{\text{fbr}}(x))\mathbb{c}_{\text{wp}} : \left[\mathbb{I} + \bar{\mathbb{P}}_{\text{wp}}^{\text{fbr}}(x) : (\mathbb{c}_{\text{wp}} - \bar{\mathbb{c}}_{\text{fbr}}(x)) \right]^{-1} \\
 & : \left\{ f_{\text{fbr}}(x)\mathbb{I} + (1 - f_{\text{fbr}}(x)) \left[\mathbb{I} + \bar{\mathbb{P}}_{\text{wp}}^{\text{fbr}}(x) : (\mathbb{c}_{\text{wp}} - \bar{\mathbb{c}}_{\text{fbr}}(x)) \right]^{-1} \right\}^{-1}.
 \end{aligned} \tag{7}$$

250 In this way, the main difference between tendon and bone at this scale was accounted for
 251 by considering a linearly varying volume fraction across the interphase (*i.e.*, $1 - f_{\text{fbr}}(x)$ with
 252 $x \in \{0, 1\}$) for their corresponding inclusion (*endotenon* for $x = 0$ or *lacuna* for $x = 1$).

253 *D. Mesostructural level – partially mineralized tissue*

254 Similarly to the microstructural level, a different modeling approach was used for the tendon
 255 and bone to account for their differences in structure and composition at the mesostructural
 256 level (step 6). On the one hand, a bundle of parallel fascicles with an interfascicular matrix
 257 (*endotenon*) forms the tendon [41]. Considering a bundle of parallel fascicles as a matrix
 258 and *endotenon* as a cylindrical inclusion, the effective stiffness tensor of tendon can be
 259 estimated. On the other hand, cortical bone hosts cylindrical pores called haversian canals,
 260 which contain the bone’s nerve and blood supplies being embedded into the osteonal lamella

261 matrix (extravascular bone) [37]. The effective stiffness tensor of cortical bone can thus be
 262 estimated by considering haversian canals as a cylindrical inclusion coated with a continuous
 263 bone matrix.

264 As in step 5, the effective stiffness tensors of a partially mineralized tissue, $\mathbb{C}_{\text{meso}}(x)$, can
 265 be estimated by considering $\mathbb{C}^0 \equiv \mathbb{C}_{\text{end}} \equiv \mathbb{C}_{\text{hav}} \equiv \mathbb{C}_{\text{wp}}$,

$$\begin{aligned} \mathbb{C}_{\text{meso}}(x) = & f_{\text{mic}}(x)\mathbb{C}_{\text{mic}}(x) + (1 - f_{\text{mic}}(x))\mathbb{C}_{\text{wp}} : \left[\mathbb{I} + \mathbb{P}_{\text{wp}}^{\text{mic}}(x) : (\mathbb{C}_{\text{wp}} - \mathbb{C}_{\text{mic}}(x)) \right]^{-1} \\ & : \left\{ f_{\text{mic}}(x)\mathbb{I} + (1 - f_{\text{mic}}(x)) \left[\mathbb{I} + \mathbb{P}_{\text{wp}}^{\text{mic}}(x) : (\mathbb{C}_{\text{wp}} - \mathbb{C}_{\text{mic}}(x)) \right]^{-1} \right\}^{-1}. \end{aligned} \quad (8)$$

266 Again, the variation across the interphase was here driven by the a linearly varying volume
 267 fraction, $1 - f_{\text{mic}}(x)$, for their corresponding inclusion only.

268 3. Model parameters

269 Like for any other hierarchical material, the knowledge of the mechanical properties and
 270 volume fractions of the tendon-to-bone insertion's elementary components, along with the
 271 competing gradients in collagen fibers organization and mineral content, are required to
 272 assess its overall mechanical behavior. A broad range of values for the mechanical properties
 273 (*e.g.*, Young's modulus E and Poisson's ratio ν) of the nanoscale components has been
 274 reported in the literature, based on experimental testing facilities or molecular dynamics
 275 (MD) simulations.

276 Earlier theoretical studies provided values of around 2 GPa for the Young's modulus of
 277 collagen, but recent MD simulations reported higher values for the Young's modulus of a
 278 single collagen molecule, ranging from 7 to 19 GPa [33]. The Poisson's ratio of collagen
 279 has typically been chosen equal to 0.28 to deliver a Poisson's ratio of around 0.35 for the
 280 collagen-water composite (recall step 1) [18, 17]. Furthermore, HA minerals were typically
 281 assumed to have a linear elastic and isotropic behavior, with a Young's modulus ranging
 282 from 63 to 165 GPa, and a Poisson's ratio of around 0.23 [33]. To date, little is known about
 283 the mechanical properties of NCPs. Nevertheless, water-NCPs composite has generally
 284 been assumed to have isotropic properties with a Young's modulus ranging from 1.3 MPa
 285 to 0.7 GPa, and a Poisson's ratio ranging from 0.4999 to 0.45, thus encompassing typical

286 values for water (*i.e.*, a nearly incompressible material with a bulk modulus of 2.2 GPa) and
 287 soft polymers [17]. The mechanical properties range of each nanoscale component used as
 input values in our multiscale model is summarized in Tab. 1.

Material	Young's modulus, E (GPa)	Poisson's ratio, ν (-)
Collagen molecules	1.2 – 9.6	0.23 – 0.33
HA minerals	63 – 165	0.18 – 0.28
Water-NCPs composite	0.0013 – 0.7	0.4999 – 0.45

Table 1: Mechanical properties range of the nanoscale components used for modeling the mesoscale effective stiffness tensor of the tendon-to-bone insertion in this study.

288
 289 A volume fraction of mineral $f_{HA}(x)$ varying linearly from 0 to 65% was considered
 290 (see Fig. 2a), based on the experimentally observed mineral concentration gradient at the
 291 tendon-to-bone insertion [26]. Moreover, the collagen fibers distribution $s(x)$ was chosen
 292 according to experimental data [42], which reported that the angular deviation values for
 293 the tendon-to-bone insertion reached a peak in the non-mineralized fibrocartilaginous region
 and varied little beyond it (see Fig. 2b)

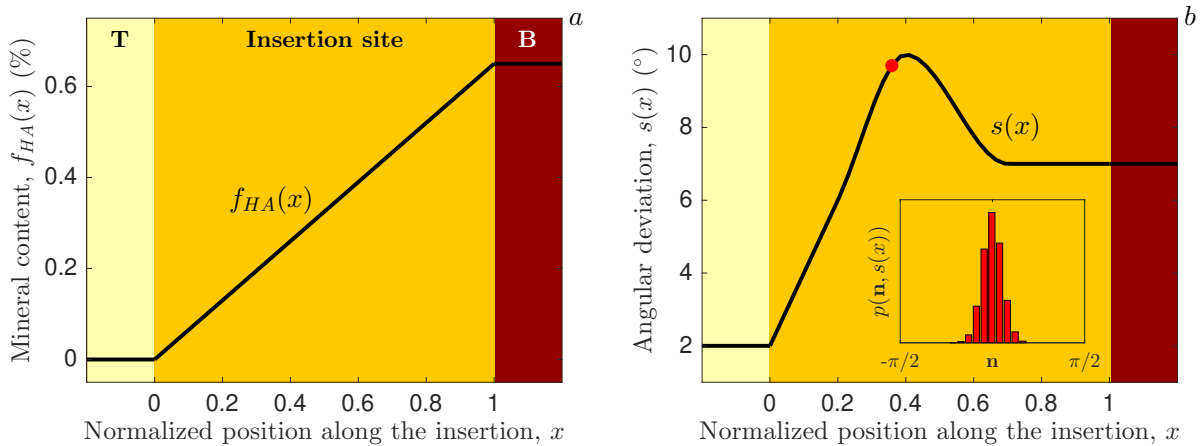


Figure 2: Spatially varying properties of the interphase from the tendon (T) to bone (B) based on competing gradients in (a) mineral content and (b) collagen fibers organization. The insert displays the distribution of collagen fibers near the region of largest fibers disorganization (red dot). These trends are based upon data reported in Refs. [22, 24].

295 The volume fractions of each phase, along with the different homogenization methods
 296 applied at each step, are summarized in Tab. 2. At the nanostructural level, the volume
 297 fraction for the water-protein mixture, f_{wp} , has been taken according to [17]. At the nanos-
 298 tructural and sub-microstructural levels, we used the values for a mineralization inside and
 299 outside the fibrils as a function of the total mineral content, *i.e.*, f_{Hw} and $1 - f_{\text{fib}}$, following
 300 the work of Nikolov and Raabe [17]. In this way, these concurrent variations lead to an
 301 overall volume fraction of mineral varying from 0 to 52% between tendon and bone at the
 302 mesoscale, which is in good agreement with values reported in the literature [16, 17]. Fur-
 303 thermore, to account for the difference in structure and composition of the tendon and bone
 304 at the micro- and mesostructural levels, volume fractions that vary linearly with respect to
 305 the normalized position x across the interphase, *i.e.*, $1 - f_{\text{fbr}}(x)$ and $1 - f_{\text{mic}}(x)$, have been
 306 considered for their respective inclusions at each of these two levels [16, 20].

Hierarchical levels	Steps	Homogenization schemes		Phases	Volume fractions (%)	Relations
Nano	1	Mori-Tanaka	Inclusion Matrix	Water-NCPs Collagen	$f_{\text{wp}} = 35$	Eq. (2)
	2	Self-consistent	Phase 1 Phase 2	Water-NCPs HA	$f_{\text{HA}}(x) = 65x$	Eq. (3)
	3	Mori-Tanaka	Inclusion Matrix	Intra-HA foam Wet collagen	$f_{\text{Hw}} = 43$	Eq. (4)
Sub-micro	4	Mori-Tanaka	Inclusion Matrix	Collagen fibril Extra-HA foam	$f_{\text{fib}} = 73$	Eq. (5)
Micro	5	Inverse Mori-Tanaka	Inclusion Matrix	Endotenon – Lacunae Collagen fiber	$f_{\text{fbr}}(x) = 8x + 90$	Eqs. (6-7)
Meso	6	Inverse Mori-Tanaka	Inclusion Matrix	Endotenon – Haversian Fascicle – Lamella	$f_{\text{mic}}(x) = 8x + 90$	Eq. (8)

Table 2: Volume fractions of each phase along with the different homogenization schemes applied at each step of the multiscale modeling.

307 **4. Numerical results**

308 The effective stiffness properties of the tendon-to-bone insertion from the nanostructural to
 309 the mesostructural levels were estimated using the six homogenization steps described in
 310 Fig. 1. Three analyses were conducted to rate the performance of the proposed multiscale
 311 model. First, several characteristics of the effective stiffness coefficients obtained at the
 312 mesostructural level (step 6) were assessed. Second, a parametric study was performed to
 313 evaluate the impact of the input parameters on the resulting effective stiffness tensor. Third,
 314 an optimization procedure was proposed to identify the model parameters that yielded the
 315 best agreement between modeled and measured effective stiffness tensors.

316 *4.1. Effective stiffness tensor at the mesostructural level, $\mathbb{C}_{meso}(x)$*

317 Figure 3 depicts the effective stiffness coefficients of the tendon-to-bone insertion obtained
 318 at the mesostructural level, together with the Voigt-Reuss bounds calculated according to
 319 [43], using the average mechanical properties from Tab. 1. Note that Voigt notation is
 320 adopted to define the coefficients of the fourth-order stiffness tensor and that the x_3 -axis
 321 denotes the longitudinal axis, which is aligned with the mean direction of the collagen fibers
 distribution (recall step 4 of Fig. 1).

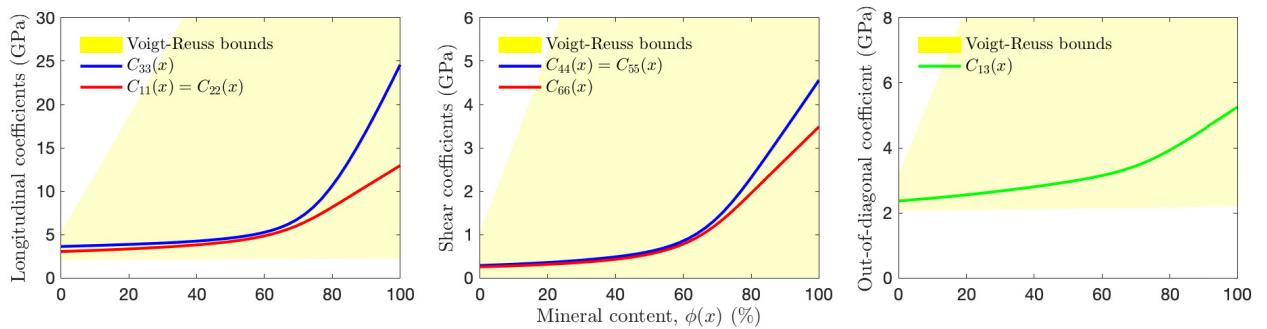


Figure 3: Effective stiffness coefficients (in Voigt notation) of the tendon-to-bone insertion obtained at the mesostructural level (continuous lines), along with the Voigt-Reuss bounds (yellow area), using the average mechanical properties from Tab. 1.

322
 323 First, it is worth pointing out that our model led to a transversely isotropic elastic be-
 324 havior for the insertion site at the mesoscale, where the stiffness coefficients along the fibers

325 (*i.e.*, $C_{33}(x)$ and $C_{44}(x)$) were consistently larger than those normal to the fibers (*i.e.*, $C_{11}(x)$
 326 and $C_{66}(x)$), thus retaining the symmetry class of the two surroundings tissues. Recalling
 327 that the main constituent properties at the nanoscale were all considered as linear elastic and
 328 isotropic, the anisotropy at the different scales was initially triggered by the consideration of
 329 geometric features (*i.e.*, the shape of the inclusion) in step 1. Second, the derived effective
 330 stiffness tensors at the extremities of the insertion, *i.e.*, $\mathbb{C}_{\text{meso}}(x = 0)$ and $\mathbb{C}_{\text{meso}}(x = 1)$ from
 331 Eq. (8), were in good agreement with experimental values reported in the literature for
 332 the Achilles tendon [44, 45] and cortical bone, measured at the tibia mid-diaphysis [46] and
 333 femoral diaphysis [47]. Third, the derived stiffness profile across the interphase was nonlin-
 334 ear, displaying a smooth stiffness increase in the non-mineralized fibrocartilaginous region
 335 ($\phi(x) < 50\%$) followed by a sudden rise in stiffness in the mineralized fibrocartilaginous
 336 region ($\phi(x) > 50\%$). The fact that an increase in mineral accumulation within collagen
 337 fibers can provide significant stiffening of the enthesis, but only for concentration of minerals
 338 above a certain percolation threshold (*i.e.*, $\phi(x) \approx 60\%$), corroborates earlier results and
 339 confirms that our model can account for effects of nonuniform mineral accumulation [22].
 340 Finally, it should be noted that the obtained stiffness coefficients all fall within the lower
 341 and upper limits defined by the Voigt-Reuss bounds.

342 4.2. Parametric study

343 The predicted output values of our multiscale model strongly depend on the mechanical prop-
 344 erties of the nanoscale components, which showed a rather high dispersion among different
 345 studies (recall Tab. 1). We thus performed a parametric study to assess the impact of these
 346 input parameters on the values of the resulting effective stiffness tensor at the mesostruc-
 347 tural level. The obtained bounds for each of the five independent stiffness coefficients are
 348 depicted in Fig. 4. As can be observed, the mechanical properties of the water-NCPs com-
 349 posite inclusion were mostly responsible for relative variations of the shear coefficients (*i.e.*,
 350 $C_{44}(x)$ and $C_{66}(x)$) in the low-mineralized region, whereas they barely affected the longitu-
 351 dinal coefficients. The mechanical properties of the collagen molecules matrix significantly
 352 affected all stiffness coefficients over the entire tendon-to-bone transition. As expected, the

353 mechanical properties of HA minerals were only responsible for variations of the stiffness
 354 coefficients in the highly mineralized region.

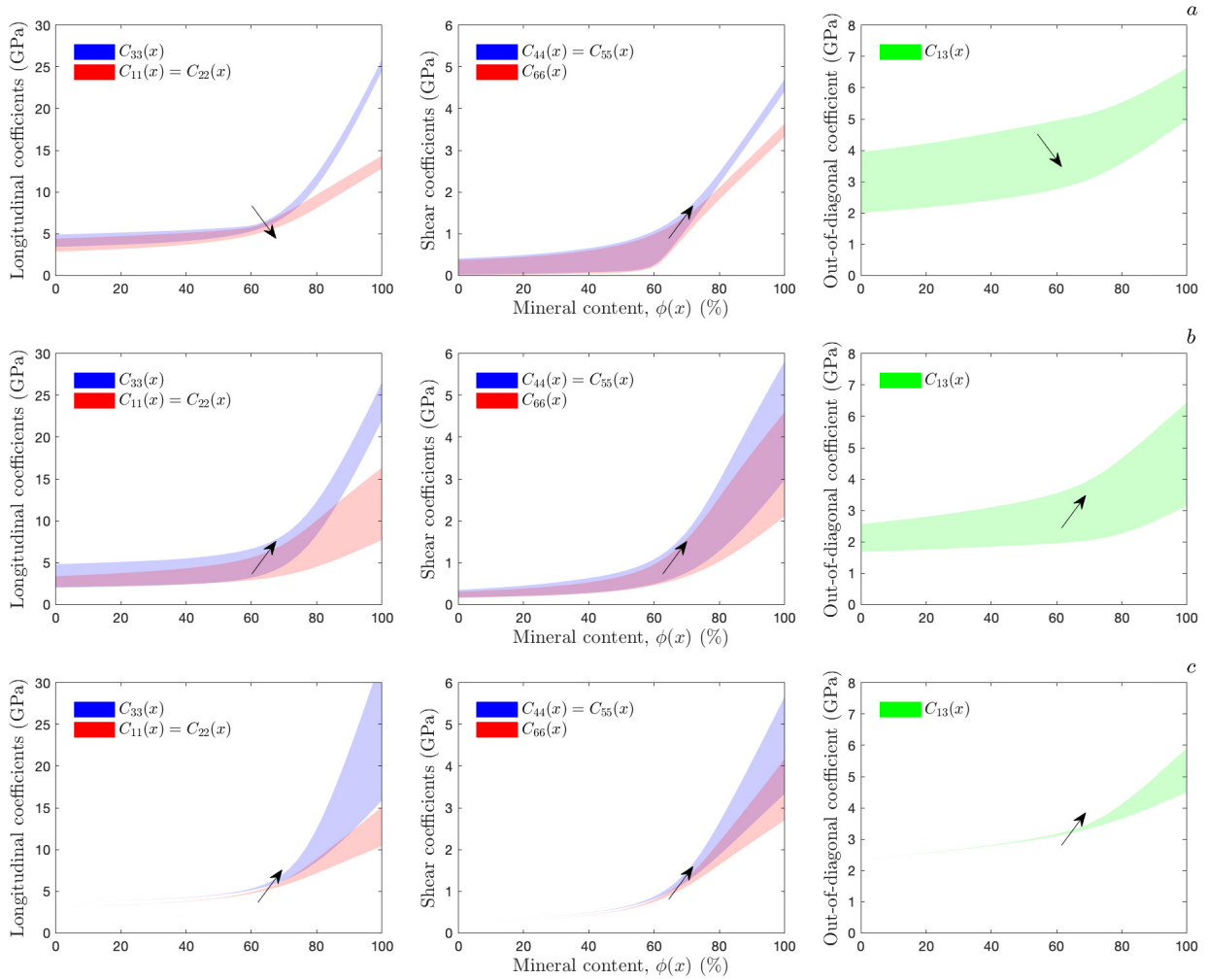


Figure 4: Stiffness coefficients bounds of the tendon-to-bone insertion at the mesostructural level for a variation of the mechanical properties of the nanoscale components: (a) water-NCPs composite; (b) collagen molecules; and (c) HA minerals. Black arrows indicate the resulting trends in stiffness with respect to increasing nanoscale properties.

355 4.3. Identification procedure

356 To further investigate the sensitivity of the effective stiffness tensor across the interphase,
 357 which, in turn, reflects the ability of our model to predict experimentally observed data,
 358 we proposed an optimization procedure to identify the model parameters θ (*i.e.*, the six

359 nanoscale properties from Tab. 1) that yielded the best agreement between modeled and
 360 measured effective stiffness tensors at the mesostructural scale, denoted by $\mathbb{C}_{\text{meso}}(\boldsymbol{\theta}; x)$ and
 361 $\mathbb{C}^{\text{exp}}(x)$, respectively. Since experimental data for the interphase at the tissue scale are not
 362 available in the literature, the optimization was conducted on data from the two surrounding
 tissues only, *i.e.*, $\mathbb{C}^{\text{exp}}(x = 0)$ and $\mathbb{C}^{\text{exp}}(x = 1)$, which are summarized in Tab. 3.

Material	Position	Stiffness tensor $\mathbb{C}^{\text{exp}}(x)$					Reference
		C_{11}^{exp}	C_{33}^{exp}	C_{13}^{exp}	C_{55}^{exp}	C_{66}^{exp}	
Tendon	$x = 0$	3.08	4.51	3.10	0.04	0.02	[44]
Cortical bone	$x = 1$	14.79	26.64	6.31	5.52	3.65	[46]

Table 3: Reference stiffness coefficients (in GPa) for tendon and bone at the mesostructural scale.

363
 364 Formally, the optimal model parameters $\hat{\boldsymbol{\theta}}$ result from the minimization of an objective
 365 function $F(\boldsymbol{\theta})$ in a least-squares sense as,

$$\hat{\boldsymbol{\theta}} = \arg \min_{\boldsymbol{\theta} \in \Theta} F(\boldsymbol{\theta}) \quad \text{with} \quad F(\boldsymbol{\theta}) = \frac{1}{N} \sum_{n=1}^N \left(\frac{C_n^{\text{exp}} - C_n(\boldsymbol{\theta})}{C_n^{\text{exp}}} \right)^2, \quad (9)$$

366 where \mathbf{C}^{exp} and $\mathbf{C}(\boldsymbol{\theta})$ are vectors that contain the measured and modeled stiffness coeffi-
 367 cients, respectively, N is the number of stiffness coefficients, and Θ denotes the bounds of the
 368 model parameters $\boldsymbol{\theta}$, which were taken according to Tab. 1. Genetic algorithms were applied
 369 to solve Eq. (9) owing to their ability in finding a near global solution for non-convex multi-
 370 dimensional objective functions, without the need of an accurate initial guess for the model
 371 parameters [48]. For this set of experimental data, the identification procedure delivered the
 372 following estimates for the model parameters, $\hat{\boldsymbol{\theta}} = [0.0153 \ 0.4991 \ 7.9 \ 0.29 \ 125.5 \ 0.23]$, which
 373 pairwise correspond to the Young's moduli (GPa) and Poisson's ratios of the water-NCPs
 374 composite, collagen molecules and HA minerals, respectively. Figure 5 depicts the optimal
 375 matching between the modeled and measured effective stiffness tensors at the mesostruc-
 376 tural scale. An excellent agreement can be observed between the modeled and measured
 377 longitudinal stiffness coefficients, with relative errors that are less than 5%. However, the
 378 agreement for the shear and out-of-diagonal stiffness coefficients was moderate for the ten-

379 don region, thus indicating that our model lacks some mechanical features that may account
 380 for a stronger anisotropy in the transverse direction.

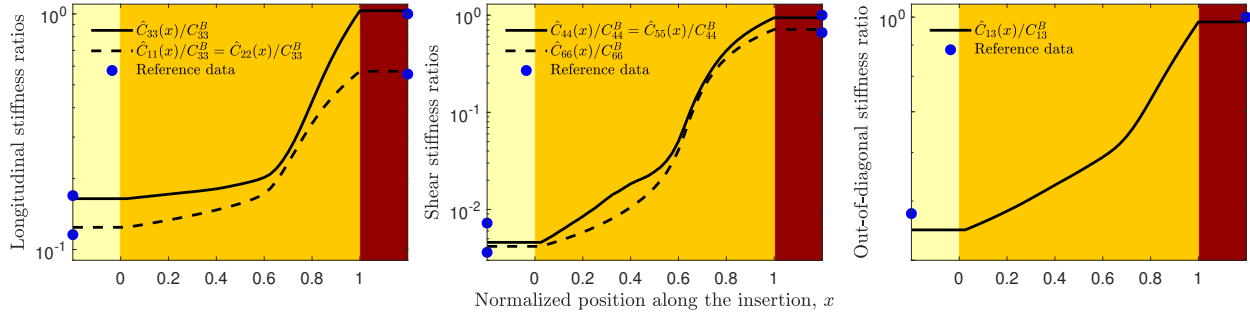


Figure 5: Optimal matching between the modeled and measured effective stiffness tensors at the mesostructural scale. Results were normalized with respect to the stiffness coefficients of bone (Tab. 3).

380

381 5. Discussion

382 The tendon-to-bone insertion plays a crucial role in the musculoskeletal system, achieving
 383 an effective transfer of mechanical stresses across two tissues displaying a substantial gap in
 384 mechanical properties of nearly two orders of magnitude. An accurate modeling accounting
 385 for the multiscale and composite nature of this interphase is essential to deepen our under-
 386 standing of complex biological interphases and has potential applications both for clinical
 387 purposes and for the development of biomimetic strategies in engineering. In this study, we
 388 proposed a multiscale model spanning four different hierarchical levels, from the nano-
 389 the mesoscale, connected based on homogenization procedures. Starting from the mechan-
 390 ical properties of the elementary nanoscale components, this multiscale modeling strategy
 391 allowed deriving the effective stiffness tensor of the enthesis at the mesoscale. Since an
 392 analytical formulation was used at every step, the computational cost of modeling was very
 393 low.

394 The main findings from this study were as follows: (1) the effective stiffness tensor across
 395 the interphase was found to be transversely isotropic at the mesostructural level (Fig. 3),
 396 thus retaining the symmetry class of the two surrounding tissues (*i.e.*, tendon and bone);
 397 (2) the mechanical properties of the elementary nanoscale components were shown to impact

398 the stiffness coefficients of the interphase at the mesoscale (Fig. 4), and were subsequently
399 optimized, by solving an inverse identification procedure, to match available ultrasonic data
400 for the two surrounding tissues (Fig. 5); and (3) our modeling results for the interphase
401 were in qualitative agreement with stochastic finite-element estimates [22, 23] and reported
402 experimental values for the insertional zones of human meniscal attachments into underlying
403 bone [49], thus supporting the hypothesis that the tendon-to-bone insertion can be seen as
404 a continuous functionally graded material.

405 Indeed, in accordance with these earlier models, our results indicated that the competing
406 gradients in mineral concentration (at the nanoscale) and collagen fibers organization (at
407 the microscale) are important factors in determining the effective mechanical behavior of
408 the tendon-to-bone insertion at the mesoscale. On the one hand, the linear increase in
409 mineral content caused a stiffening of the interphase that became significant beyond a certain
410 percolation threshold. On the other hand, the decreasing collagen fiber organization across
411 the interphase led to a reduced tissue stiffness along the main fibers direction. The existence
412 of a region that is more compliant than either tendon or bone (continuous line in Fig. 6)
413 was the result of these competing gradients. Moreover, it can be shown that the dominant
414 factors driving the width and depth of this compliant region are the onset of mineralization
415 and the angular deviation from the main collagen fibers direction (dashed line in Fig. 6).

416 Despite these promising results, mismatch observed between the model predictions and
417 experimental data (Fig. 5) could rise from simplifying hypotheses that were adopted at
418 different stages of the modeling. First, the transition between different hierarchies from the
419 nanoscale to the mesoscale is continuous rather than discrete in real biological structures [33].
420 However, a limited number of length scales was accounted for in the modeling, by assuming
421 the existence of a RVE at each scale and each normalized position across the interphase,
422 in order to fulfill the separation-of-scales requirements (*i.e.*, features at a previous scale are
423 much smaller than those at the next scale). This is not necessarily correct for the tendon-to-
424 bone insertion because the features at a previous scale may not be strictly infinitesimal with
425 respect to a larger scale. Although several continuum micromechanics approaches have been
426 used to model partially mineralized tissues with a certain success [16–20, 29, 50], their use

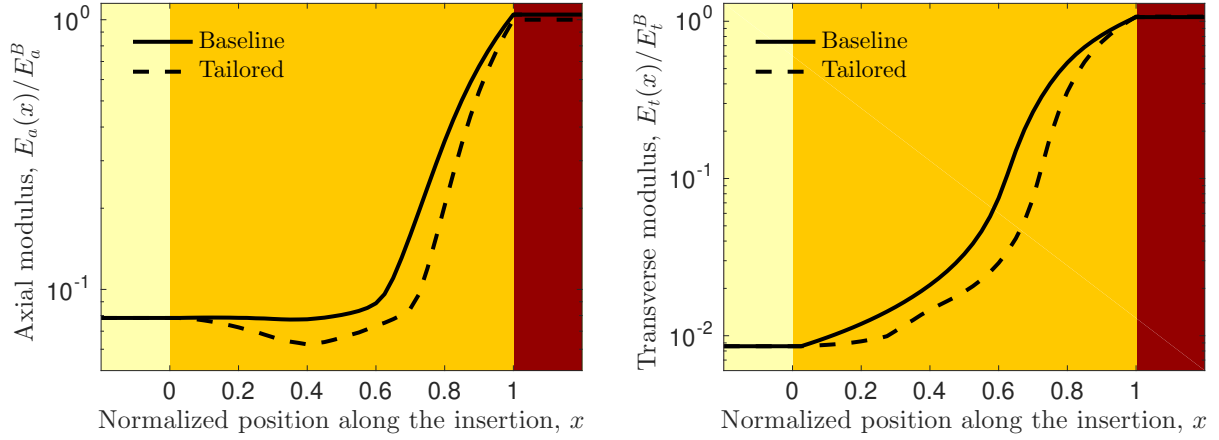


Figure 6: Mesostructural level estimates of the longitudinal elastic moduli. The baseline (continuous line) displays the axial and transverse moduli obtained from the optimal stiffness coefficients depicted in Fig. 5, whereas the tailored case (dashed line) was obtained by delaying the onset of mineralization (to $x \approx 0.2$) and reducing the collagen fibers organization (angular deviation increased to 5°).

427 at the nanoscale has sparked important discussions among the homogenization community
428 and is open to debate [51]. For instance, the nano-sized dimensions of mineralized tissue
429 components as well as their spatial arrangements and interactions motivated alternative
430 approaches based on discrete atomistic simulations, specifically molecular dynamics [52].
431 A second challenging issue was the selection of the mechanical properties of the nanoscale
432 components, *i.e.*, Young's moduli and Poisson's ratios. In this study, all nanoscale com-
433 ponents (*i.e.*, water-NCPs composite, collagen molecules and HA crystals) were assumed
434 to have a linear elastic and isotropic behavior. Wide range of values for these nanoscale
435 properties have been reported in the literature (recall Tab. 1) and different choices of such
436 properties may lead to very different results. For instance, atomistic modeling approach of
437 collagen molecules revealed that collagen may have a highly nonlinear viscoelastic behav-
438 ior [53]. Likewise, the geometry and properties of HA crystals are still subject to debate.
439 This includes the shape of the mineral particles, which have been considered both as nee-
440 dles [38, 54] or plates [5, 34]. Some evidences also shown that HA crystals may be oriented
441 randomly around the mineralized collagen fibrils [55], that their size can change during

442 the mineralization from the tendon to bone [56], or that their mechanical properties are
443 anisotropic [57]. Third, only a few studies differentiated between intra- and extrafibrillar
444 mineral volume fractions. Indeed, the mineralization of fibril arrays, in particular the ratio
445 between extra- and intrafibrillar mineral content, has sparked important discussions. Some
446 authors mentioned a high intrafibrillar mineral content [58, 59], whereas some others evi-
447 denced that the mineral content is mainly located in the extrafibrillar matrix [60, 61]. More
448 recent contributions underlined that mineralization pathways in bone are neither exclusively
449 intrafibrillar nor extrafibrillar [62], but rather form a continuous cross-fibrillar phase [38],
450 but this feature remains largely unexplored for the tendon-to-bone insertion [23]. Fourth,
451 the profiles of the competing gradients in mineral content and collagen fibers orientation
452 were selected according to earlier modeling strategies [22, 23], themselves based on Raman
453 spectroscopy [26] and polarized light microscopy [42]. Nevertheless, recent experimental
454 developments for measuring these finely tuned gradients across the interphase are likely
455 to provide different (nonlinear) profiles [63, 64], which could be used as well to feed our
456 modeling approach. Fifth, based on the considered biological phases and their interactions
457 at each scale [34, 56], different methods have been used to estimate the effective stiffness
458 tensor at each homogenization step: The Mori-Tanaka method (steps 1, 3 and 4), the self-
459 consistent method (step 2), and the “inverse Mori-Tanaka” scheme (steps 5 and 6). It is
460 commonly acknowledged that the Mori-Tanaka method shows limited performance for prob-
461 lems involving high volume fraction of inclusions over around 35% [65], since the inclusions’
462 distribution and interactions are not accounted for properly. Therefore, the attributions of
463 matrix and inclusions roles in our modeling steps 3 and 4 are open to question, so that other
464 homogenization methods could have been used. For instance, a rigorous approach has been
465 proposed for composites containing multiple classes of aligned ellipsoidal inclusions with a
466 relatively high volume fraction [24], although this scheme can violate the Hashin-Shtrikman
467 bounds at low volume fraction for certain anisotropy of the phases. Lastly, our modeling ap-
468 proach contains many steps, each of which should be validated experimentally in the future.
469 To date, little information is available in the literature concerning the experimental multi-
470 scale evaluation of the mechanical properties at the tendon-to-bone attachment. Current

471 imaging modalities have been used to map the local content of the main constituents across
472 the interphase [26, 63, 10], but a direct link with the corresponding variations in mechan-
473 ical properties is somehow still missing. Ongoing developments of experimental techniques
474 for measuring the local mechanical properties of the interphase at different scales, such as
475 nanoscale dynamic mechanical analysis [66] or scanning acoustic microscopy [67], are ex-
476 pected to provide means of comparing our numerically obtained predictions.

477 All these uncertainties along with some other model parameters ignored in this work, such
478 as the gradient in protein content [68], the different collagen types across the interphase [4]
479 or the unraveling of tendon fibers into smaller interphase fibrils [10], make the multiscale
480 modeling of the tendon-to-bone insertion a challenging problem with much potential for fu-
481 ture works. As such, the modeling process proposed here is straightforwardly extendable to
482 account for damage characteristics as a footprint of clinical burden that occur at the tendon-
483 to-bone insertion, which may include for instance the multiscale effects of unloading (*e.g.*,
484 stiffening of the HA foam at the nanoscale or fibers misalignment at the microscale) [56]. Be-
485 sides, such model paves the way to the design of bioinspired bi-materials [69] that display the
486 functionally graded properties of the enthesis, and their characterization using quantitative
487 ultrasound [70, 71].

488 6. Conclusion

489 We modeled the tendon-to-bone insertion as a hierarchical composite material and pre-
490 dicted its effective anisotropic stiffness tensor at the tissue scale. Our multiscale analysis
491 involved a bottom-up approach, starting from the nanostructural level (partially mineralized
492 collagen fibril) and then moving up the scales through the sub-microstructural level (par-
493 tially mineralized fiber), the microstructural level (pattern of partially mineralized fibers),
494 up to the mesostructural level (partially mineralized tissue level). Our modeling results sup-
495 ported the hypothesis that the tendon-to-bone insertion can be considered as a continuous
496 functionally graded material with respect to its mineral concentration and collagen fibers
497 organization, thus confirming earlier results obtained using phenomenological models (*i.e.*,
498 stochastic finite element simulations) and experimentally reported trends.

499 **Acknowledgement**

500 This work was partially funded by the BEST-AMUS project (IIN program, CNRS-INSIS),
501 the “Support for research for newly appointed Associate Professors” and the “Bonus Qualité
502 Recherche” (Faculté des Sciences et Technologie, Université Paris-Est Créteil).

503 **Appendix A. Hill tensor \mathbb{P}^0**

504 *Appendix A.1. Hill tensor for a cylindrical inclusion in a transversely isotropic medium*

The non-zero components of the Hill tensor \mathbb{P}^0 for a cylindrical inclusion embedded in a transversely isotropic matrix of stiffness \mathbb{C}^0 are given according to [72] using Voigt notation, x_3 being the axis of rotational symmetry,

$$P_{11}^0 = \frac{1}{8} \frac{(C_{22}^0 + C_{66}^0) + 2C_{66}^0}{C_{22}^0 C_{66}^0}, \quad (\text{A.1})$$

$$P_{22}^0 = \frac{1}{8} \frac{(C_{22}^0 + 3C_{66}^0)}{C_{22}^0 C_{66}^0}, \quad (\text{A.2})$$

$$P_{12}^0 = \frac{1}{8} \frac{C_{66}^0 - C_{22}^0}{C_{22}^0 C_{66}^0}, \quad (\text{A.3})$$

$$P_{66}^0 = \frac{1}{2} \frac{C_{22}^0 + C_{66}^0}{C_{22}^0 C_{66}^0}, \quad (\text{A.4})$$

$$P_{44}^0 = \frac{1}{2C_{44}^0}, \quad (\text{A.5})$$

$$P_{55}^0 = P_{44}^0. \quad (\text{A.6})$$

Considering the case of a spherical inclusion embedded in an isotropic matrix of stiffness \mathbb{C}^0 [72], the components of the Hill tensor \mathbb{P}^0 now read as

$$P_{11}^0 = \frac{7C_{44}^0 + 2C_{12}^0}{15C_{44}^0(C_{12}^0 + 2C_{44}^0)}, \quad (\text{A.7})$$

$$P_{12}^0 = \frac{C_{44}^0 + C_{12}^0}{-15C_{44}^0(C_{12}^0 + 2C_{44}^0)}, \quad (\text{A.8})$$

$$P_{44}^0 = \frac{2(3C_{12}^0 + 8C_{44}^0)}{15C_{44}^0(C_{12}^0 + 2C_{44}^0)}, \quad (\text{A.9})$$

$$P_{22}^0 = P_{33}^0 = P_{11}^0, \quad P_{55}^0 = P_{66}^0 = P_{44}^0, \quad P_{13}^0 = P_{23}^0 = P_{12}^0. \quad (\text{A.10})$$

506 **Appendix B. Effective stiffness tensor of the hydroxyapatite foam $\mathbb{C}_{\text{Hw}}(x)$**

The self-consistent scheme for two interpenetrating (spherical) inclusion phases with a linear elastic and isotropic behavior can be solved according to [32]. In such a case, the nonlinear system of equations (3) can be substituted by a system of two nonlinear equations (note that the spatial variable x was omitted here for sake of clarity),

$$\frac{f_{\text{HA}}(K_{\text{HA}} - K_{\text{Hw}})}{1 + \alpha_{\text{Hw}}(K_{\text{HA}} - K_{\text{Hw}})/K_{\text{Hw}}} + \frac{(1 - f_{\text{HA}})(K_{\text{wp}} - K_{\text{Hw}})}{1 + \alpha_{\text{Hw}}(K_{\text{wp}} - K_{\text{Hw}})/K_{\text{Hw}}} = 0, \quad (\text{B.1})$$

$$\frac{f_{\text{HA}}(G_{\text{HA}} - G_{\text{Hw}})}{1 + \beta_{\text{Hw}}(G_{\text{HA}} - G_{\text{Hw}})/G_{\text{Hw}}} + \frac{(1 - f_{\text{HA}})(G_{\text{wp}} - G_{\text{Hw}})}{1 + \beta_{\text{Hw}}(G_{\text{wp}} - G_{\text{Hw}})/G_{\text{Hw}}} = 0, \quad (\text{B.2})$$

where the two unknowns K_{Hw} and G_{Hw} denote the bulk and shear moduli of the HA foam, respectively. The parameters α_{Hw} and β_{Hw} are defined as

$$\alpha_{\text{Hw}} = \frac{3K_{\text{Hw}}}{3K_{\text{Hw}} + 4G_{\text{Hw}}}, \quad \beta_{\text{Hw}} = \frac{6(K_{\text{Hw}} + 2G_{\text{Hw}})}{5(3K_{\text{Hw}} + 4G_{\text{Hw}})}. \quad (\text{B.3})$$

Solving the aforementioned system yields the following components for the stiffness tensor of the hydroxyapatite foam,

$$C_{11}^{\text{Hw}} = K_{\text{Hw}} + \frac{4}{3}G_{\text{Hw}}, \quad (\text{B.4})$$

$$C_{12}^{\text{Hw}} = K_{\text{Hw}} - \frac{2}{3}G_{\text{Hw}}, \quad (\text{B.5})$$

$$C_{44}^{\text{Hw}} = G_{\text{Hw}}, \quad (\text{B.6})$$

$$C_{22}^{\text{Hw}} = C_{33}^{\text{Hw}} = C_{11}^{\text{Hw}}, \quad C_{13}^{\text{Hw}} = C_{23}^{\text{Hw}} = C_{12}^{\text{Hw}}, \quad C_{55}^{\text{Hw}} = C_{66}^{\text{Hw}} = C_{44}^{\text{Hw}}. \quad (\text{B.7})$$

507 References

- 508 [1] M Benjamin, T Kumai, S Milz, BM Boszczyk, AA Boszczyk, and JR Ralphs. The skeletal attachment
509 of tendons–tendon ‘entheses’. *Comp Biochem Physiol A Mol Integr Physiol*, 133(4):931–945, 2002.
- 510 [2] J Buschmann and GM Bürgisser. *Biomechanics of tendons and ligaments: tissue reconstruction and
511 regeneration*. Woodhead Publishing, 2017.
- 512 [3] J Apostolakos, TJS Durant, CR Dwyer, RP Russell, JH Weinreb, F Alaei, K Beitzel, MB McCarthy,
513 MP Cote, and AD Mazzocca. The enthesis: a review of the tendon-to-bone insertion. *Muscles Ligaments
514 Tendons J*, 4(3):333, 2014.
- 515 [4] AD Waggett, JR Ralphs, APL Kwan, D Woodnutt, and M Benjamin. Characterization of collagens
516 and proteoglycans at the insertion of the human Achilles tendon. *Matrix Biol*, 16(8):457–470, 1998.
- 517 [5] S Weiner and HD Wagner. The material bone: structure-mechanical function relations. *Annu Rev
518 Mater Sci*, 28(1):271–298, 1998.
- 519 [6] HH Lu and S Thomopoulos. Functional attachment of soft tissues to bone: development, healing, and
520 tissue engineering. *Annu Rev Biomed Eng*, 15:201–226, 2013.
- 521 [7] Y Liu, V Birman, C Chen, S Thomopoulos, and GM Genin. Mechanisms of bimaternal attachment at
522 the interface of tendon to bone. *J Eng Mater Technol*, 133(1):011006, 2011.
- 523 [8] Y Hu, V Birman, A Deymier-Black, AG Schwartz, S Thomopoulos, and GM Genin. Stochastic interdig-
524 itation as a toughening mechanism at the interface between tendon and bone. *Biophys J*, 108(2):431–437,
525 2015.
- 526 [9] SF Tellado, ER Balmayor, and M Van Griensven. Strategies to engineer tendon/ligament-to-bone
527 interface: Biomaterials, cells and growth factors. *Adv Drug Deliv Rev*, 94:126–140, 2015.
- 528 [10] L Rossetti, LA Kuntz, E Kunold, J Schock, KW Müller, H Grabmayr, J Stolberg-Stolberg, F Pfeiffer,
529 SA Sieber, R Burgkart, and AR Bausch. The microstructure and micromechanics of the tendon–bone
530 insertion. *Nat Mater*, 16(6):664, 2017.

- 531 [11] GM Genin and S Thomopoulos. The tendon-to-bone attachment: Unification through disarray. *Nat*
532 *Mater*, 16(6):607, 2017.
- 533 [12] N Felsenthal and E Zelzer. Mechanical regulation of musculoskeletal system development. *Development*,
534 144(23):4271–4283, 2017.
- 535 [13] AG Schwartz, JH Lipner, JD Pasteris, GM Genin, and S Thomopoulos. Muscle loading is necessary
536 for the formation of a functional tendon enthesis. *Bone*, 55(1):44–51, 2013.
- 537 [14] F Saadat, AC Deymier, V Birman, S Thomopoulos, and GM Genin. The concentration of stress at the
538 rotator cuff tendon-to-bone attachment site is conserved across species. *J Mech Behav Biomed Mater*,
539 62:24–32, 2016.
- 540 [15] GS Jung and MJ Buehler. Multiscale modeling of muscular-skeletal systems. *Annu Rev Biomed Eng*,
541 19:435–457, 2017.
- 542 [16] A Fritsch and C Hellmich. ‘Universal’ microstructural patterns in cortical and trabecular, extracellular
543 and extravascular bone materials: micromechanics-based prediction of anisotropic elasticity. *J Theor*
544 *Biol*, 244(4):597–620, 2007.
- 545 [17] S Nikolov and D Raabe. Hierarchical modeling of the elastic properties of bone at submicron scales:
546 the role of extrafibrillar mineralization. *Biophys J*, 94(11):4220–4232, 2008.
- 547 [18] YJ Yoon and SC Cowin. The estimated elastic constants for a single bone osteonal lamella. *Biomech*
548 *Model Mechanobiol*, 7(1):1–11, 2008.
- 549 [19] E Hamed, I Jasiuk, A Yoo, Y Lee, and T Litzka. Multi-scale modelling of elastic moduli of trabecular
550 bone. *J R Soc Interface*, 9(72):1654–1673, 2012.
- 551 [20] S Tiburtius, S Schrof, F Molnár, P Varga, F Peyrin, Q Grimal, K Raum, and A Gerisch. On the elastic
552 properties of mineralized turkey leg tendon tissue: multiscale model and experiment. *Biomech Model*
553 *Mechanobiol*, 13(5):1003–1023, 2014.
- 554 [21] EM Spiesz and PK Zysset. Structure–mechanics relationships in mineralized tendons. *J Mech Behav*
555 *Biomed Mater*, 52:72–84, 2015.
- 556 [22] GM Genin, A Kent, V Birman, B Wopenka, JD Pasteris, PJ Marquez, and S Thomopoulos. Functional
557 grading of mineral and collagen in the attachment of tendon to bone. *Biophys J*, 97(4):976–985, 2009.
- 558 [23] Y Liu, S Thomopoulos, C Chen, V Birman, MJ Buehler, and GM Genin. Modelling the mechanics of
559 partially mineralized collagen fibrils, fibres and tissue. *J R Soc Interface*, 11(92):20130835, 2014.
- 560 [24] F Saadat, V Birman, S Thomopoulos, and GM Genin. Effective elastic properties of a composite
561 containing multiple types of anisotropic ellipsoidal inclusions, with application to the attachment of
562 tendon to bone. *J Mech Phys Solids*, 82:367–377, 2015.
- 563 [25] AC Deymier, Y An, JJ Boyle, AG Schwartz, V Birman, GM Genin, S Thomopoulos, and AH Barber.
564 Micro-mechanical properties of the tendon-to-bone attachment. *Acta Biomater*, 56:25–35, 2017.

- 565 [26] B Wopenka, A Kent, JD Pasteris, Y Yoon, and S Thomopoulos. The tendon-to-bone transition of the
566 rotator cuff: a preliminary raman spectroscopic study documenting the gradual mineralization across
567 the insertion in rat tissue samples. *Appl Spectrosc*, 62(12):1285–1294, 2008.
- 568 [27] A Zaoui. Continuum micromechanics: survey. *J Eng Mech*, 128(8):808–816, 2002.
- 569 [28] JD Eshelby. The determination of the elastic field of an ellipsoidal inclusion, and related problems.
570 *Proc R Soc Lond A*, 241(1226):376–396, 1957.
- 571 [29] D Gagliardi, V Sansalone, C Desceliers, and S Naili. Estimation of the effective bone-elasticity tensor
572 based on μ CT imaging by a stochastic model. a multi-method validation. *Eur J Mech A-Solid*, 69:147–
573 167, 2018.
- 574 [30] T Mori and K Tanaka. Average stress in matrix and average elastic energy of materials with misfitting
575 inclusions. *Acta Metall*, 21(5):571–574, 1973.
- 576 [31] R Hill. A self-consistent mechanics of composite materials. *J Mech Phys Solids*, 13(4):213–222, 1965.
- 577 [32] C Hellmich, J-F Barthélémy, and L Dormieux. Mineral–collagen interactions in elasticity of bone
578 ultrastructure—a continuum micromechanics approach. *Eur J Mech A Solids*, 23(5):783–810, 2004.
- 579 [33] E Hamed, Y Lee, and I Jasiuk. Multiscale modeling of elastic properties of cortical bone. *Acta Mech*,
580 213(1-2):131–154, 2010.
- 581 [34] B Alexander, TL Daulton, GM Genin, J Lipner, JD Pasteris, B Wopenka, and S Thomopoulos. The
582 nanometre-scale physiology of bone: steric modelling and scanning transmission electron microscopy of
583 collagen–mineral structure. *J R Soc Interface*, 9(73):1774–1786, 2012.
- 584 [35] J Orgel, TC Irving, A Miller, and TJ Wess. Microfibrillar structure of type I collagen in situ. *Proc*
585 *Natl Acad Sci*, 103(24):9001–9005, 2006.
- 586 [36] P Fratzl, HS Gupta, EP Paschalis, and P Roschger. Structure and mechanical quality of the collagen–
587 mineral nano-composite in bone. *J Mater Chem*, 14(14):2115–2123, 2004.
- 588 [37] A Fritsch, C Hellmich, and L Dormieux. Ductile sliding between mineral crystals followed by rupture of
589 collagen crosslinks: experimentally supported micromechanical explanation of bone strength. *J Theor*
590 *Biol*, 260(2):230–252, 2009.
- 591 [38] N Reznikov, M Bilton, L Lari, MM Stevens, and R Kröger. Fractal-like hierarchical organization of
592 bone begins at the nanoscale. *Science*, 360(6388):eaao2189, 2018.
- 593 [39] P Kannus. Structure of the tendon connective tissue. *Scand J Med Sci Sports*, 10(6):312–320, 2000.
- 594 [40] E Hamed, E Novitskaya, J Li, P-Y Chen, I Jasiuk, and J McKittrick. Elastic moduli of untreated,
595 demineralized and deproteinized cortical bone: validation of a theoretical model of bone as an inter-
596 penetrating composite material. *Acta Biomater*, 8(3):1080–1092, 2012.
- 597 [41] CT Thorpe, KJ Karunaseelan, J Ng Chieng Hin, GP Riley, HL Birch, PD Clegg, and HRC Screen.
598 Distribution of proteins within different compartments of tendon varies according to tendon type. *J*

- 599 *Anat*, 229(3):450–458, 2016.
- 600 [42] S Thomopoulos, JP Marquez, B Weinberger, V Birman, and GM Genin. Collagen fiber orientation at
601 the tendon to bone insertion and its influence on stress concentrations. *J Biomech*, 39(10):1842–1851,
602 2006.
- 603 [43] J Qu and M Cherkaoui. *Fundamentals of micromechanics of solids*. Wiley Online Library, 2006.
- 604 [44] BK Hoffmeister, SM Handley, SA Wickline, and JG Miller. Ultrasonic determination of the anisotropy
605 of Young’s modulus of fixed tendon and fixed myocardium. *J Acoust Soc Am*, 100(6):3933–3940, 1996.
- 606 [45] J Brum, M Bernal, JL Gennisson, and M Tanter. In vivo evaluation of the elastic anisotropy of the
607 human Achilles tendon using shear wave dispersion analysis. *Phys Med Biol*, 59(3):505, 2014.
- 608 [46] S Bernard, J Schneider, P Varga, P Laugier, K Raum, and Q Grimal. Elasticity–density and
609 viscoelasticity–density relationships at the tibia mid-diaphysis assessed from resonant ultrasound spec-
610 troscopy measurements. *Biomech Model Mechan*, 15(1):97–109, 2016.
- 611 [47] X Cai, H Follet, L Peralta, M Gardegaront, D Farlay, R Gauthier, B Yu, E Gineyts, C Olivier, M Langer,
612 A Gourrier, D Mitton, F Peyrin, Q Grimal, and P Laugier. Anisotropic elastic properties of human
613 femoral cortical bone and relationships with composition and microstructure in elderly. *Acta Biomater*,
614 90:254–266, 2019.
- 615 [48] N Bochud, J Laurent, F Bruno, D Royer, and C Prada. Towards real-time assessment of anisotropic
616 plate properties using elastic guided waves. *J Acoust Soc Am*, 143(2):1138–1147, 2018.
- 617 [49] KN Hauch, ML Oyen, GM Odegard, and TL Haut Donahue. Nanoindentation of the insertional zones
618 of human meniscal attachments into underlying bone. *J Mech Behav Biomed Mater*, 2(4):339–347,
619 2009.
- 620 [50] D Gagliardi, S Naili, C Desceliers, and V Sansalone. Tissue mineral density measured at the sub-
621 millimetre scale can provide reliable statistics of elastic properties of bone matrix. *Biomech Model
622 Mechan*, 16(6):1885–1910, 2017.
- 623 [51] E Hamed and I Jasiuk. Elastic modeling of bone at nanostructural level. *Mater Sci Eng R Rep*,
624 73(3-4):27–49, 2012.
- 625 [52] MJ Buehler. Molecular nanomechanics of nascent bone: fibrillar toughening by mineralization. *Nan-
626 otechnology*, 18(29):295102, 2007.
- 627 [53] A Gautieri, S Vesentini, A Redaelli, and MJ Buehler. Viscoelastic properties of model segments of
628 collagen molecules. *Matrix Biol*, 31(2):141–149, 2012.
- 629 [54] S Von Euw, T-H-C Chan-Chang, C Paquis, G Haye, Band Pehau-Arnaudet, F Babonneau, T Azais,
630 and N Nassif. Organization of bone mineral: The role of mineral–water interactions. *Geosciences*,
631 8(12):466, 2018.
- 632 [55] MA Rubin, I Jasiuk, J Taylor, J Rubin, T Ganey, and RP Apkarian. TEM analysis of the nanostructure

- 633 of normal and osteoporotic human trabecular bone. *Bone*, 33(3):270–282, 2003.
- 634 [56] AC Deymier, AG Schwartz, Z Cai, TL Daulton, JD Pasteris, GM Genin, and S Thomopoulos. The
635 multiscale structural and mechanical effects of mouse supraspinatus muscle unloading on the mature
636 enthesis. *Acta Biomater*, 83:302–313, 2019.
- 637 [57] JL Katz and K Ukraincik. On the anisotropic elastic properties of hydroxyapatite. *J Biomech*, 4(3):221–
638 227, 1971.
- 639 [58] S Weiner and W Traub. Organization of hydroxyapatite crystals within collagen fibrils. *FEBS letters*,
640 206(2):262–266, 1986.
- 641 [59] N Sasaki and Y Sudoh. X-ray pole figure analysis of apatite crystals and collagen molecules in bone.
642 *Calcif Tissue Int*, 60(4):361–367, 1997.
- 643 [60] N Sasaki, A Tagami, T Goto, M Taniguchi, M Nakata, and K Hikichi. Atomic force microscopic studies
644 on the structure of bovine femoral cortical bone at the collagen fibril-mineral level. *J Mater Sci: Mater*,
645 13(3):333–337, 2002.
- 646 [61] EA McNally, HP Schwarcz, GA Botton, and AL Arsenault. A model for the ultrastructure of bone
647 based on electron microscopy of ion-milled sections. *PLOS one*, 7(1):e29258, 2012.
- 648 [62] M Georgiadis, R Müller, and P Schneider. Techniques to assess bone ultrastructure organization:
649 orientation and arrangement of mineralized collagen fibrils. *J R Soc Interface*, 13(119):20160088, 2016.
- 650 [63] JP Spalazzi, AL Boskey, N Pleshko, and HH Lu. Quantitative mapping of matrix content and distri-
651 bution across the ligament-to-bone insertion. *PLoS One*, 8(9):e74349, 2013.
- 652 [64] D Qu, SD Subramony, AL Boskey, N Pleshko, SB Doty, and HH Lu. Compositional mapping of the
653 mature anterior cruciate ligament-to-bone insertion. *J Orthop Res*, 35(11):2513–2523, 2017.
- 654 [65] HM Yin, LZ Sun, and Glaucio H Paulino. Micromechanics-based elastic model for functionally graded
655 materials with particle interactions. *Acta Mater*, 52(12):3535–3543, 2004.
- 656 [66] I Zlotnikov, E Zolotoyabko, and P Fratzl. Nano-scale modulus mapping of biological composite mate-
657 rials: Theory and practice. *Prog Mater Sci*, 87:292–320, 2017.
- 658 [67] S Leicht and K Raum. Acoustic impedance changes in cartilage and subchondral bone due to primary
659 arthrosis. *Ultrasonics*, 48(6-7):613–620, 2008.
- 660 [68] S Thomopoulos, GR Williams, JA Gimbel, M Favata, and LJ Soslowsky. Variation of biomechanical,
661 structural, and compositional properties along the tendon to bone insertion site. *J Orthop Res*,
662 21(3):413–419, 2003.
- 663 [69] MJ Mirzaali, AH de la Nava, D Gunashekar, M Nouri-Goushki, RPE Veeger, Q Grossman, L Angeloni,
664 MK Ghatkesar, LE Fratila-Apachitei, D Ruffoni, EL Doubrovski, and AA Zadpoor. Mechanics of
665 bioinspired functionally graded soft-hard composites made by multi-material 3D printing. *Compos*
666 *Struct*, page 111867, 2020.

- 667 [70] N Bochud, Q Vallet, J-G Minonzio, and P Laugier. Predicting bone strength with ultrasonic guided
668 waves. *Sci Rep*, 7:43628, 2017.
- 669 [71] G Rosi, L Placidi, V-H Nguyen, and S Naili. Wave propagation across a finite heterogeneous interphase
670 modeled as an interface with material properties. *Mech Res Commun*, 84:43–48, 2017.
- 671 [72] AP Suvorov and GJ Dvorak. Rate form of the Eshelby and Hill tensors. *Int J Solids Struct*, 39(21-
672 22):5659–5678, 2002.